ACS APPLIED MATERIALS & INTERFACES

www.acsami.org

Research Article

Real-Space Infrared Spectroscopy of Ferroelectric Domain Walls in Multiferroic *h*-(Lu,Sc)FeO_3

Kevin A. Smith, Sriram P. Ramkumar, Kai Du, Xianghan Xu, Sang-Wook Cheong, Stephanie N. Gilbert Corder, Hans A. Bechtel, Elizabeth A. Nowadnick, and Janice L. Musfeldt*

Cite This: *ACS Appl. Mater. Interfaces* 2023, 15, 7562–7571

Read Online

ACCESS | Metrics & More | Article Recommendations | Supporting Information

ABSTRACT: We employ synchrotron-based near-field infrared spectroscopy to image the phononic properties of ferroelectric domain walls in hexagonal (*h*) $Lu_{0.6}Sc_{0.4}FeO_3$, and we compare our findings with a detailed symmetry analysis, lattice dynamics calculations, and prior models of domain-wall structure. Rather than metallic and atomically thin as observed in the rare-earth manganites, ferroelectric walls in *h*-$Lu_{0.6}Sc_{0.4}FeO_3$ are broad and semiconducting, a finding that we attribute to the presence of an *A*-site substitution-induced intermediate phase that reduces strain and renders the interior of the domain wall nonpolar. Mixed Lu/Sc occupation on the *A* site also provides compositional heterogeneity over micron-sized length scales, and we leverage the fact that Lu and Sc cluster in different ratios to demonstrate that the spectral characteristics at the wall are robust even in different compositional regimes. This work opens the door to broadband imaging of physical and chemical heterogeneity in ferroics and represents an important step toward revealing the rich properties of these flexible defect states.

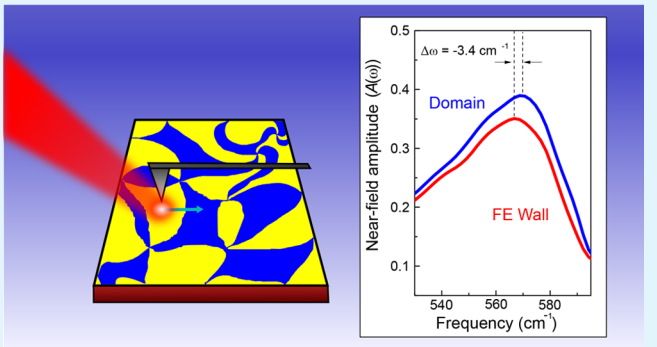

KEYWORDS: *ferroelectricity, domain walls, symmetry analysis, near-field infrared imaging, orthoferrites*

INTRODUCTION

Ferroelectric domain walls are usually considered to be atomically thin. There are numerous piezo force and conducting atomic force microscopy measurements of hexagonal rare-earth manganites, demonstrating that the interlocked structural antiphase and ferroelectric domain walls that combine to form cloverleaf-like vortices have essentially zero width.[1−6] As predicted by Fennie and Rabe,[7] improper ferroelectricity in the hexagonal rare-earth manganites is induced by a Mn center buckling distortion.[8,9] The subsequent discovery of collective alternating net magnetization at cross-coupled domain walls[10,11] showed that interacting ferroelectric and magnetic domains (or walls) are key to understanding giant response mechanisms in many multiferroics. That walls have essentially zero width was verified theoretically by Kumagai and Spaldin,[12] who studied two different models of domain walls in $YMnO_3$. The first was an atomically thin ferroelectric wall, and the second was a wider wall with an intermediate $P\bar{3}c1$ phase that effectively endows the interface with nonpolar character. Because the energy of the atomically thin ferroelectric wall is lower than that of the wider, two-phase domain wall, we should anticipate ferroelectric domain walls of essentially zero width in the rare-earth manganites and related materials.[12] While manganites are the archetype for fundamental studies of domain-wall properties,[13] many other materials, including complex chalcogenides,[14,15] lead perovskites,[16] and spin-crossover complexes,[17] host these structures, making it of great fundamental interest to image the phononic properties of these interfaces. At the same time, ferroelectric hafnia benefits from ultralow barriers to topological domain-wall switching[18] and wake-up and fatigue processes in $(Hf_{0.5}Zr_{0.5})O_2$ are connected with reversible domain-wall transitions and O center movement,[19] providing powerful reminders of the practical importance of these processes.

It is obviously quite challenging to image the properties of an interface with vanishing width. We therefore decided to explore a possible exception to this general case by taking advantage of the domain walls created by *A*-site substitution, hexagonal (*h*) $Lu_{0.6}Sc_{0.4}FeO_3$.[20,21] Tunneling electron microscopy was utilized to map the ferroelectric domains previously, but unlike infrared spectroscopy, it does not reveal the vibrational properties of domain walls. In addition to being a

Received: October 31, 2022
Accepted: January 9, 2023
Published: January 30, 2023

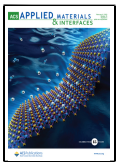

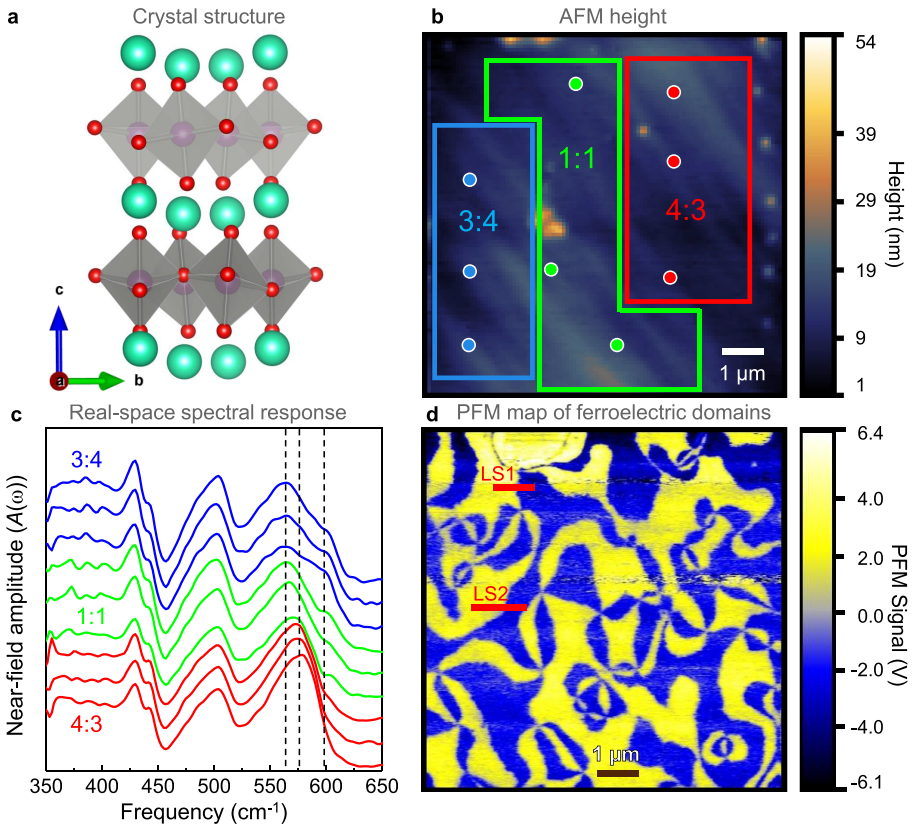

Figure 1. Overview of chemical and physical heterogeneity in *h*-$Lu_{0.6}Sc_{0.4}FeO_3$. (a) Crystal structure of the unit cell of *h*-$Lu_{0.6}Sc_{0.4}FeO_3$. The space group is $P6_3cm$.[21] Teal, purple, and red spheres represent Lu/Sc sites, Fe atoms, and O atoms, respectively. (b) Atomic force microscopy (AFM) showing the topography of an area of interest, with marks indicating the location of point spectra. (c) Point spectra corresponding to the locations indicated in part b. Curves are labeled and colored to match the different types of spectra observed in the various local composition areas. (d) Piezo force microscopy of the ferroelectric vortex domains over the same area scanned in part b. Red lines show the positions of line scan 1 (LS1) and line scan 2 (LS2) taken in the 1:1 and 3:4 compositional regions, respectively.

more suitable platform for our infrared imaging techniques, this system provides an opportunity to revisit predicted wall structures[12] and to explore precisely how the local structure relaxes across a ferroelectric domain wall.

Ferrites generally adopt either an orthorhombic or hexagonal crystal symmetry depending on the radius of the *A*-site ion.[22] $LuFeO_3$ normally hosts an orthorhombic structure, although the pure hexagonal phase can be stabilized under epitaxial strain.[23] Similarly, *A*-site substitution with Sc, the smallest and lightest of the Group III elements, leads to a more compact lattice, which favors the hexagonal structure (Figure 1a). This is due to chemical pressure effects, which give rise to local strain.[21,24] *h*-$Lu_{0.6}Sc_{0.4}FeO_3$ is ferroelectric at room temperature, providing ample opportunity to study ferroelectric domain walls at ambient conditions. At the same time, disorder and inhomogeneity are known to modify the overall width and number of domain walls.[25] Like the hexagonal rare-earth manganites, *h*-$Lu_{0.6}Sc_{0.4}FeO_3$ is an improper ferroelectric with a polar distortion induced by buckling of the bipyramidal layers and Lu/Sc distortion in a trimerized fashion.[26,27] This system thus hosts two order parameters: the polar and so-called K_3 trimer distortions. Piezo force microscopy reveals a cloverleaf pattern of micron-sized vortex ferroelectric domains in the single crystals,[21] similar to those in the manganites.[28] These ferroelectric domain walls are also structural antiphase boundaries due to rotating O distortions.[21] Further analysis reveals two types of ferroelectric walls: one variety has FeO_5 dimers, and the other kind does not.[3] Low-temperature magnetic force microscopy demonstrates that the weak ferromagnetic domains are distinct from the ferroelectric domains in terms of size and shape and that there exists no mutual locking between their domain walls.[21] These findings suggest decoupling between ferroelectricity and weak ferromagnetism in this system.[9] Domain walls have also been observed by scanning tunneling electron microscopy in related systems such as $(LuFeO_3)_m(LuFe_2O_4)_n$ superlattices.[29]

Although sensitive techniques have been developed for macroscopic measurements of magnetoelectric coupling,[28,30] there remains a need to detect properties within a single domain or at a domain wall.[10,11,20] Vibrational spectroscopies are well-suited for unveiling the phonons that drive polar displacements in a ferroelectric material and exposing the microscopic origin of phononic properties such as thermal conductivity, specific heat, and thermal expansion.[31] As a reminder, ferroelectricity requires a broken inversion center, and infrared spectroscopy, with the ability to measure odd-symmetry vibrational modes, is the perfect method for revealing how symmetry evolves across a ferroelectric domain wall. Traditional infrared spectroscopy is not suitable because it cannot be focused beyond the diffraction limit $d = \lambda/2NA$, where λ is the wavelength of light and NA is the size of the numerical aperture. This means that 500 cm^{-1} light has a diffraction-limited spot size of 10 μm or greater, far too large to image topological objects like domain walls. Synchrotron-

https://doi.org/10.1021/acsami.2c19600
ACS Appl. Mater. Interfaces 2023, 15, 7562−7571

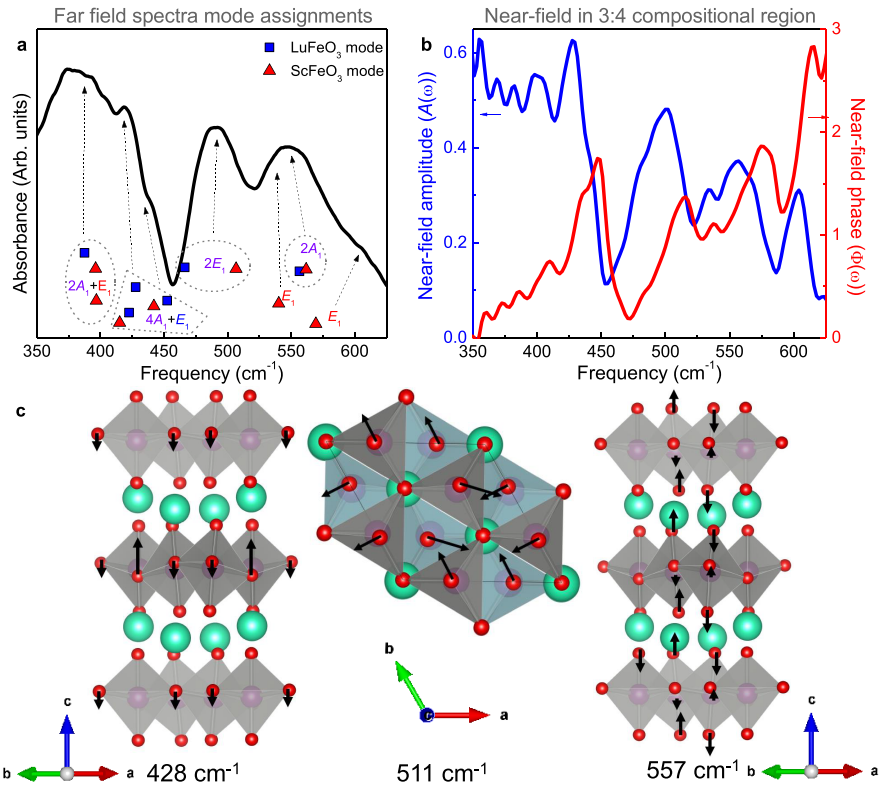

Figure 2. Comparison of far- and near-field infrared spectra of h-$Lu_{0.6}Sc_{0.4}FeO_3$. The (a) far-field infrared spectrum and (b) near-field amplitude and phase are in good agreement. We assign the features of the near-field spectrum based on our complementary lattice dynamics calculations shown in panel a. The theoretical modes are given by blue squares or red triangles for Lu- or Sc-containing modes, respectively. Both frequencies and relative intensities are indicated. This figure focuses on the frequency range of the near-field response. (c) Three selected mode displacement patterns (at 428, 511, and 557 cm^{-1}, computed for $LuFeO_3$). Displacement patterns calculated for $ScFeO_3$ are the same but with slightly higher frequencies.

based near-field infrared nanospectroscopy offers a way forward as the 20 nm spatial resolution overcomes the diffraction limit and provides the sensitivity needed to measure samples with small lateral area.[32−34] Furthermore, the recent extension into the far-infrared is ideal for complex oxides.[35] We recently employed this technique to explore strain relief and order parameter trends across ferroelastic walls in the hybrid improper ferroelectric $Ca_3Ti_2O_7$.[36] We imaged wide ferroelastic walls but were unable to resolve signatures of ferroelectric walls in crystals mapped with piezo force microscopy, likely because they were too thin. Several related materials such as $Ca_3(Ti_{0.1}Ru_{0.9})_2O_7$ and $(Ca_{0.99}Sr_{0.01})_2RuO_4$ host ferroelastic domain walls with significant widths as well,[37,38] demonstrating that there are other systems of contemporary interest with macroscopic walls.

In order to advance the understanding of these fascinating topological defect states, we combine the wider ferroelectric domain walls in h-$Lu_{0.6}Sc_{0.4}FeO_3$ (induced by A-site substitution) with synchrotron-based near-field infrared nanospectroscopy and compare our results with complementary lattice dynamics calculations and a symmetry analysis. Not only can we image the ferroelectric domain walls in this system for the first time, but we find that the structural relaxation is surprisingly wide, at least from a local structure point of view. In addition to near-field amplitude changes across the walls, we detect small frequency shifts. We have long sought evidence for mode hardening and softening at both ferroelastic and ferroelectric walls, but in our prior work,[36] the predicted frequency shifts of the phonon modes were below our sensitivity. Now we can use these frequency shifts to revisit the question of whether there could be a nonpolar structure embedded inside the ferroelectric wall[12] or whether the wall remains polar all the way through. We also take advantage of the natural compositional gradient due to A-site substitution to study the wall behavior in slightly different chemical environments, providing an early glimpse of chemical tuning opportunities. This work opens the door to broadband imaging of physical and chemical heterogeneity in ferroics and represents an important step to revealing the rich properties of these flexible defect states for ultralow power memory and computing devices.[39−41] More generally, Z_6 topological vortex domain structures are related to contemporary issues in quantum information (e.g., clock model, graph theory) as well as cosmology (the Kibble−Zurek mechanism, which describes the possible formation of topological defects during a spontaneous symmetry-breaking phase transition at the birth of the universe).[1,42,43] Physical manifestations of these models in the form of domain-wall interfaces in ferroic oxides are therefore very attractive objects to explore.

RESULTS AND DISCUSSION

A-Site Substitution and Compositional Variation in the Spectroscopic Response. As a prelude to our near-field measurements of domain walls in h-$Lu_{0.6}Sc_{0.4}FeO_3$, we studied A-site substitution effects, the statistics of Lu and Sc occupation (best visualized as "red and blue balls" on 14

https://doi.org/10.1021/acsami.2c19600
ACS Appl. Mater. Interfaces 2023, 15, 7562−7571

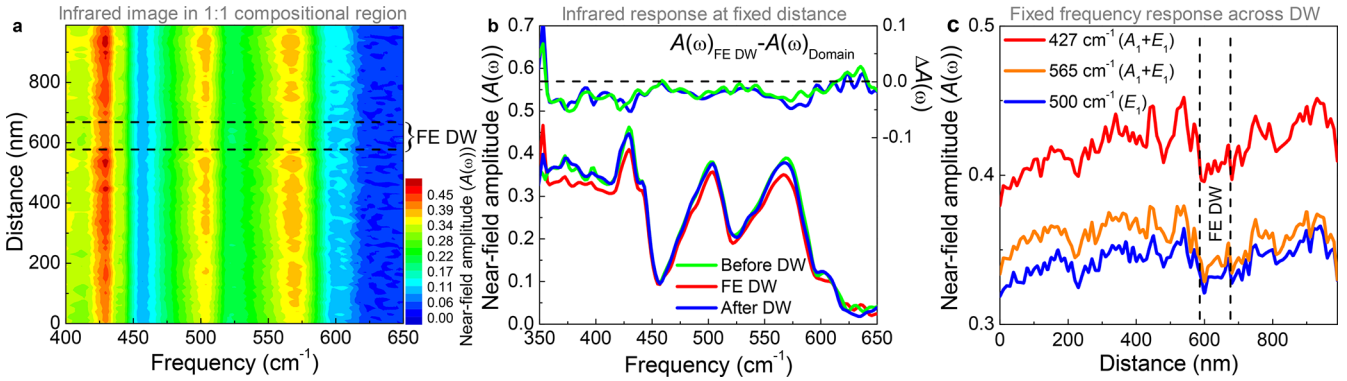

Figure 3. Near-field infrared response across a ferroelectric domain wall (FE DW) in *h*-$Lu_{0.6}Sc_{0.4}FeO_3$. (a) Color contour plot presents the near-field infrared response as a function of the distance across a ferroelectric domain wall, indicated by the horizontal dashed lines, in the 1:1 Lu/Sc compositional region. The image corresponds to LS1 in Figure 1d. The spatial resolution is 20 × 20 nm^2, and the spectrum is sampled every 10 nm along the line scan. The color indicates near-field amplitude, as shown by the scale bar. (b) Constant distance curves, extracted from the real-space infrared image in panel a. Cuts are taken before, after, and at the ferroelectric domain wall. Difference spectra [$A(\omega)$ at the wall − $A(\omega)$ away from the wall] are shown at the top of this panel. (c) Fixed frequency cuts of the image in panel a. These data reveal how the near-field amplitude evolves as a function of the distance at the indicated frequencies, which correspond to particular vibrational modes. The frequencies are selected to provide contrast at the ferroelectric domain wall in the 1:1 Lu/Sc compositional regime.

sites), and the impact of compositional heterogeneity on the spectroscopic response. By combining multiple techniques, we are able to place size constraints on the different compositional regions observed in *h*-$Lu_{0.6}Sc_{0.4}FeO_3$. This heterogeneity is a consequence of the local structure and depends on the relative abundance of Lu and Sc (henceforth, the Lu/Sc ratio). What we find is that the global and local Lu/Sc ratios are different. The crystal structure of *h*-$Lu_{0.6}Sc_{0.4}FeO_3$ is shown in Figure 1a. It consists of a layer of corner-sharing FeO_5 bipyramids between the hexagonal slabs containing the Lu and Sc centers. We initially performed traditional infrared microscopy in order to understand the size of these compositional regions. Even using a 20 × 20 μm^2 aperture—close to the resolution limit for this method due to the diffraction limit of light—these measurements reveal no obvious differences. We therefore conclude that the composition varies across much smaller length scales.

At the same time, we clearly observe different spectral responses using near-field techniques. Here, the spatial resolution is many orders of magnitude smaller (20 nm) due to the tip-enhanced nature of the method.[34] By sampling different areas on the surface, we are also able to identify different compositional regions that are significantly larger than the tip (Figure 1b). We therefore conclude that the compositional domains in *h*-$Lu_{0.6}Sc_{0.4}FeO_3$ are smaller than what can be measured with a far-field technique but also larger than the spatial resolution of a near-field point scan. We estimate that the length scale of compositional variation is 1−3 μm (Figure 1b), similar to those of other heterogeneous materials.[44] Moreover, each region hosts a slightly different spectroscopic response (Figure 1c). This mapping process allows the topography and position be correlated with the composition.

As established above, the spectral differences observed on the micron scale are due to the natural compositional variation in the sample. Because *h*-$Lu_{0.6}Sc_{0.4}FeO_3$ is stabilized in the hexagonal phase (as confirmed by X-ray diffraction), we know that the Lu/Sc ratio has to be between 4:3 and 3:4.[21] This implies that there are three principle compositional variants: 4:3, 1:1, and 3:4. On its surface, this is a standard case of understanding how *A*-site substitution and chemical inhomogeneity appear in and stabilize *h*-$Lu_{0.6}Sc_{0.4}FeO_3$. The distinguishing aspect of our work is how we combine this analysis with infrared imaging of the ferroelectric domain walls, linking both chemical and physical heterogeneity.

Because of the Lu versus Sc mass difference, the Sc-rich areas display features at slightly higher frequencies. This general expectation explains the variations in Figure 1b,c and is justified by a detailed comparison of the mode frequencies in $LuFeO_3$ versus $ScFeO_3$ (Tables S1 and S2). As a result, we can assign Lu/Sc ratios based on the simplest models consistent with observed spectral shapes. Recall that there are three choices for crystals in the hexagonal phase: 4:3, 1:1, and 3:4. The spectra collected from the blue region in Figure 1b and plotted in Figure 1c display the most prominent high-frequency features. Specifically, the prominence of the peak at 600 cm^{-1}, which is primarily associated with O displacements calculated for $ScFeO_3$, is the key signature of this region, and we attribute it to the highest local Sc concentration and a Lu/Sc ratio of 3:4. Likewise, the region in green has prominent features at higher frequency compared to the red area, so we assign the local Lu/Sc ratios in these regions as 1:1 and 4:3, respectively. We can therefore identify the local Lu/Sc ratio by subtle differences in the shape of the local near-field infrared response.

Vibrational-Mode Assignments and Lattice Dynamics Calculations. Figure 2 displays the absorption of *h*-$Lu_{0.6}Sc_{0.4}FeO_3$ measured by far-field techniques, the synchrotron-based near-field infrared spectrum (both amplitude and phase), and the results of our complementary lattice dynamics calculations. We confine our attention to the region between 350 and 650 cm^{-1}, where we have prominent features. Figure 2c shows representative phonon displacement patterns that occur near these frequencies. By inspecting the displacement patterns, we find that phonons near 430 cm^{-1} have fairly complex patterns that combine bond stretching and bending. The mode at 428 cm^{-1} consists of primarily equatorial O displacements, where within each bipyramid two O atoms displace down and the third displaces up by twice the amount (or two up, one down). This is reminiscent of the up−up−down *A*-site cation displacements found in these materials. The displacement patterns of phonons with frequencies near 510

https://doi.org/10.1021/acsami.2c19600
ACS Appl. Mater. Interfaces 2023, 15, 7562−7571

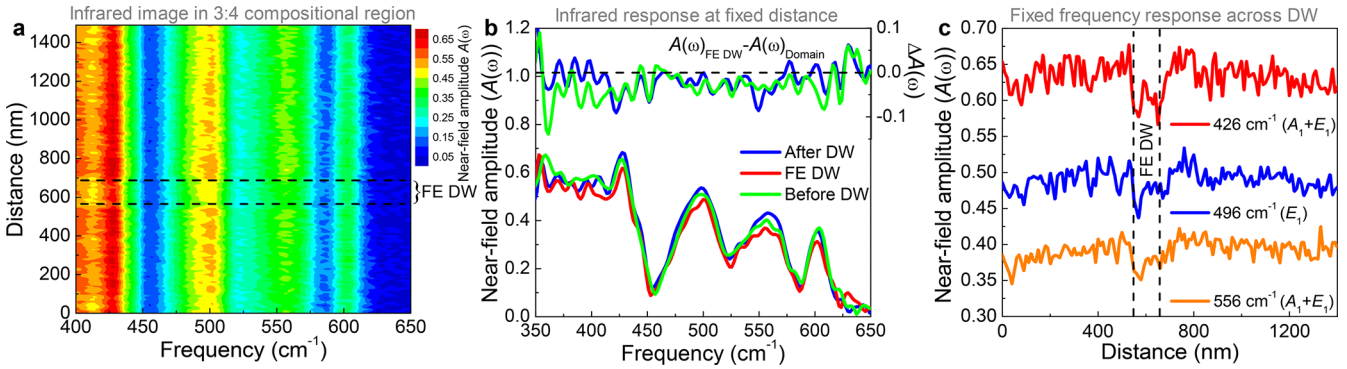

Figure 4. Near-field infrared response across a ferroelectric domain wall (FE DW) in h-$Lu_{0.6}Sc_{0.4}FeO_3$. (a) Color contour plot presenting the near-field infrared response as a function of the distance across a ferreoelectric domain wall, as indicated by the horizontal dashed lines, in the 3:4 Lu/Sc compositional region. The image corresponds to LS2 in Figure 1d. The spatial resolution is 20 × 20 nm^2, and the spectrum is sampled every 10 nm along the line scan. The color indicates near-field amplitude, as shown by the scale bar. (b) Constant distance curves, extracted from the real-space infrared image in panel a. Cuts are taken before, after, and at the ferroelectric domain wall. Difference spectra [$A(\omega)$ at the wall − $A(\omega)$ away from the wall] are shown at the top of this panel. (c) Fixed frequency cuts of the image in panel a. These data reveal how the near-field amplitude evolves as a function of the distance at the indicated frequencies, which correspond to particular vibrational modes. The frequencies are selected to provide contrast at the ferroelectric domain wall in the 3:4 Lu/Sc compositional region.

cm^{-1} involve primarily bending of the Fe−O bonds, arising mainly from apical O displacements. Finally, the phonons near 560 cm^{-1} consist primarily of Fe−O bond stretches. The vibrational modes that directly contain Lu and Sc motion as part of their displacement patterns resonate below 300 cm^{-1}, outside of the detector range. On the other hand, A-site chemistry does provide indirect or "proximity effects" to the FeO_5-related stretching and bending modes as we discuss below. A full set of mode assignments including experimental + calculated frequencies and symmetries are given in the Supporting Information. With the mode assignments of h-$Lu_{0.6}Sc_{0.4}FeO_3$ on a firm foundation, we are ready to image the ferroelectric domain walls.

Near-Field Infrared Imaging of Ferroelectric Domain Walls. Beyond spectral changes due to compositional heterogeneity, h-$Lu_{0.6}Sc_{0.4}FeO_3$ hosts polar domains with ferroelectric walls that separate these domains. The walls in this system are unusually thick, probably due to A-site substitution. While having polarization "up" or "down" (Figure 1d) does not create spectral contrast in and of itself, there is infrared contrast at the interface. This is because symmetry is broken at the wall since polarization either has to rotate (Néel wall) or turn off and on (Ising wall). Local compositional defects (such as O deficiencies and perhaps the smaller Sc^{3+} ions) also tend to migrate to the walls.[45,46] In any case, the walls that we seek to image are extremely small, so a far-field measurement with a large beam will provide only an average response.[47] Tip-enhanced techniques are needed to (i) beat the diffraction limit and (ii) reveal the properties of individual walls.

We locate ferroelectric domain walls of interest in h-$Lu_{0.6}Sc_{0.4}FeO_3$ with a multistep procedure. We begin by measuring atomic and piezo force microscopy on a flat area of a crystal according to the natural topography present in both fields of view. The results of this process are provided in Figure 1b,d. Navigation is made easier by proximity to gold markers. In order to reposition ourselves near specific domain walls at the beamline, we perform additional atomic force microscopy to map the surface in the same field of view as was previously mapped with piezo force microscopy. This assures proper positioning of the tip for a near-field line scan. Details are available in the Methods section and Supporting Information.

Figure 3 displays the real-space infrared response of a ferroelectric domain wall taken wholly within the 1:1 Lu/Sc compositional domain of h-$Lu_{0.6}Sc_{0.4}FeO_3$ along with fixed position and fixed frequency cuts of the image. There are three primary findings. First, the phononic signature of the domain wall has lower near-field amplitude compared to the surrounding area. Second, the extent of the spectral response spans roughly 100 nm, indicating that local structural aspects of the wall as measured by infrared spectroscopy are anomalously wide.[48−50] Third, the walls are semiconducting rather than metallic, as evidenced by the strong phonon response and lack of a Drude signature. This is different from the conducting atomic force microscopy results in the literature,[51−53] although several of the more recent studies emphasize that the region of the domain wall is simply more conducting than the surroundings rather than metallic.[20,54−58] We verify these findings by examining a ferroelectric domain wall in a different compositional region as described below.

Figure 4 summarizes the synchroton-based near-field infrared response of a different ferroelectric domain wall. This one is fully within the 3:4 Lu/Sc compositional domain, and again it includes the contour plot as well as fixed position and fixed frequency cuts of the image. Certain similarities are immediately apparent, although there are significant differences as well. For instance, a line scan across the wall reveals clear phonons the entire time, an indication that the wall is insulating. The width of the wall in LS2 (120 nm) is slightly wider than that in LS1, and again we see a diminished near-field amplitude at the wall. Because domain walls relieve the strain between domains, the energy is minimized if the system is allowed to relax over a wider range.[59,60] We attribute the width of the response to this relaxation.[36] This is different from the atomically thin walls reported previously.[48−50] We hypothesize that that Sc^{3+} (the small A-site ion) and O may be migrating to the defect,[61] thus creating larger distortions and broader structural relaxations.

Frequency Shifts at the Ferroelectric Domain Walls. In addition to amplitude and width changes, near-field infrared spectroscopy reveals that there are subtle frequency shifts of

https://doi.org/10.1021/acsami.2c19600
ACS Appl. Mater. Interfaces 2023, 15, 7562−7571

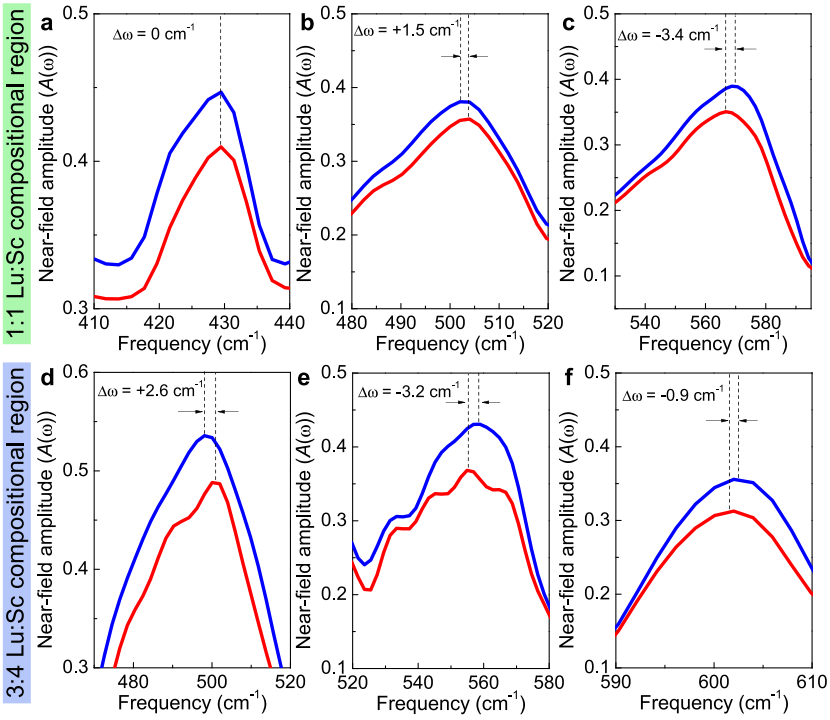

Figure 5. Close-up view of the frequency shifts at the ferroelectric domain walls. Data are taken (a–c) within the 1:1 Lu/Sc compositional region and (d–f) from the 3:4 Lu/Sc compositional region. Spectra are collected at (red curves) and away from (blue curves) the domain wall to emphasize the frequency shifts associated with the wall.

the phonon modes at the walls. While predicted in the past,[62,63] experimental evidence has been lacking, even though we have been searching for these signatures for some time. Resolving these changes is quite challenging because the expected frequency shifts are small, and the resolution that we employ in the near-field line scans (8 cm^{-1}) is traditionally not very high. As a result, the frequency shifts that we find in *h*-$Lu_{0.6}Sc_{0.4}FeO_3$ are at the limit of our sensitivity. Even so, frequency shifts, both bending and stretching modes, are observed in nearly all of the phonons. Figure 5 summarizes our findings.

Focusing first on the bending modes of *h*-$Lu_{0.6}Sc_{0.4}FeO_3$, we see that wall phonons are nearly identical with those in the nearby ferroelectric domains. For instance, none of the O–Fe–O bending modes shift at the wall in the 1:1 or 3:4 Lu/Sc compositional regimes. The Fe–O stretching modes are more interesting. The response of the wall in the 3:4 Lu/Sc region is the most significant, with frequency shifts on the order of +2.6, −3.2, and −0.9 cm^{-1} for the stretching modes near 498, 559, and 602 cm^{-1}, respectively. These are significant frequency shifts, suggesting the possibility that the ferroelectric domain walls in the 3:4 Lu/Sc compositional region of *h*-$Lu_{0.6}Sc_{0.4}FeO_3$ may have a different internal structure than the surroundings, akin to the higher-energy structure proposed by Kumagai and Spaldin in ref 12. While these frequency shifts are not precise enough to tease out the intermediate space group inside the domain wall as we have done with *h*-$Lu_{0.6}Sc_{0.4}FeO_3$ under pressure,[27] they are consistent with the overall picture of using a structural modification to minimize strain across a relatively wide wall. Frequency shifts of the 504 and 568 cm^{-1} Fe–O stretching modes at the wall in the 1:1 Lu/Sc compositional region are also significant at +1.5 and −3.4 cm^{-1}, respectively. If these frequency shifts could be augmented by near-field data at lower frequencies, it might be possible to compare calculations of the hexagonal, $P\bar{3}c1$, and $P6_3/mmc$ structures to see if predicted frequency shifts across the wall are consistent with the measurements. Such a comparison could, in principle, reveal the nature of an intermediate phase that might allow a wide domain wall to host a nonpolar interior. Finally, we point out that, based on these frequency shifts, the force constants change by 1 or 2% at the interface. Both softening and hardening are observed.

CONCLUSIONS

In this work, we combined synchrotron-based near-field infrared nanospectroscopy, a detailed symmetry analysis, and lattice dynamics calculations to reveal the properties of a quasi-one-dimensional topological object in the form of a ferroelectric domain wall. These studies are enabled by the development of broadband infrared imaging with nanometer-scale spatial resolution and the thick domain walls in $Lu_{0.6}Sc_{0.4}FeO_3$, where thanks to *A*-site substitution, we also explore how local stoichiometry variations impact the response. Contrary to the expectation for atomically sharp conducting domain walls, we find semiconducting walls with wide local lattice distortions that act to minimize strain. Further, the phonon frequency shifts across the ferroelectric domain walls are consistent with the appearance of an intermediate (possibly nonpolar) phase internal to the wall, in line with models studied by Kumagai and Spaldin.[12] Looking ahead, ferroelectric domain walls of the type discussed in this work will find application in emerging logic and memory technologies. Naturally, properties like thermal conductivity and heat capacity are key to effective heat management, and useful microscopic models of dissipation require information about the fundamental excitations of the lattice at the wall in addition to wall-induced scattering.[64] These findings open the door to phononic engineering of

https://doi.org/10.1021/acsami.2c19600
ACS Appl. Mater. Interfaces 2023, 15, 7562–7571

domain-wall-based device architectures, where strategies to create bespoke behavior by altering the local chemistry significantly extend the complexity of these efforts.

METHODS

Crystal Growth, Characterization, and Mapping. High-quality *h*-$Lu_{0.6}Sc_{0.4}FeO_3$ single crystals were grown using optical floating zone techniques as described previously.[21] X-ray diffraction was used to confirm the hexagonal phase, and the lack of peak broadening confirmed the quality of the single crystals.[21] We mounted the crystal to expose the *ab*-plane surface for microscopy measurements and used gold markers to determine the location. Both atomic and piezo force microscopies were performed at room temperature to associate the surface topology with the shape and position of the polar domains. We located each region of interest using this gold marker−topological−polar domain map and selected near-field line scans to cross features of interest as described below. For all of the piezo force microscopy measurements, 5 V alternating-current at 68 kHz was applied to a tip [a commercial conductive antiferromagnetic (AFM) tip], while the sample backside was grounded. We also employed near-field infrared spectroscopy to explore the chemical heterogeneity in *h*-$Lu_{0.6}Sc_{0.4}FeO_3$ and delineate compositional boundaries. These images were overlaid with topography and polarity information to perform line scans within different compositional ranges.

Synchrotron-Based Near-Field Spectroscopy. Near-field infrared measurements were carried out at Beamline 2.4 of the Advanced Light Source at Lawrence Berkeley National Laboratory.[34,35] Here, a commercial Neaspec IR-neaSCOPE instrument was coupled to a customized Ge:Cu detector with a KRS5 or Si beamsplitter (330−800 cm^{-1}; 8 cm^{-1} resolution).[35] A PtSi tip with a 25 nm radius was used to achieve the 20 × 20 nm^2 spatial resolution. Second-harmonic near-field amplitude $A(\omega)$ and phase $\Phi(\omega)$ were obtained simultaneously. We focused primarily on the near-field amplitude because it is most strongly related to traditional reflectance. Line scans of various lengths were carried out in order to cross between different polar domains and, by so doing, traverse a ferroelectric wall. Spectra were sampled every 10 nm on each line scan. By oversampling in real space, we improved the spatial resolution and signal-to-noise ratios. The area of interest was mapped with atomic force microscopy before and after each line scan to check for sample drift. All of these experiments were done at room temperature.

Traditional Far-Field Infrared Spectroscopy. Complementary far-field measurements were performed using a suite of spectrometers in our laboratory (including a Bruker 113v Fourier transform infrared spectrometer equipped with a helium-cooled bolometer and an Equinox 55 equipped with an attached infrared microscope) over the 20−7000 cm^{-1} frequency range. Far-field spectroscopy was used to confirm the spectral shape and mode assignments. It was also employed to place constraints on the size of the compositional domains in *h*-$Lu_{0.6}Sc_{0.4}FeO_3$. The spatial resolution of the infrared microscope was on the order of 20 × 20 μm^2, several orders of magnitude larger than that of our near-field measurements. This difference was used to support our analysis of the chemical heterogeneity.

Density Functional Theory (DFT) Calculations. We performed DFT calculations using the projector-augmented-wave method, as implemented in *VASP*[65] on the end-member compounds $LuFeO_3$ and $ScFeO_3$. To treat the electronic correlations on Fe, we employed the Liechtenstein et al.[66] formulation of DFT+*U*, with on-site Coulomb and exchange parameters U = 4.5 eV and J = 0.95 eV. An A-type antiferromagnetic (A-AFM) order was imposed on the Fe spins. We used the PBEsol functional, a 600 eV plane-wave energy cutoff, and a 4 × 4 × 2 Γ-centered *k*-point mesh. For structural relaxation, forces were converged to 2 meV/Å. We used density functional perturbation theory (DFPT)[67] to compute the Γ-point phonon frequencies, Born effective charge tensors ($Z^*_{\kappa,\alpha\beta}$ for atom κ and displacement directions α and β = 1−3), and eigendisplacements ($X_{\kappa,\beta}$). Using these quantities, we calculated the infrared intensity of phonon mode m using Phonopy[68,69] and the Phonopy−Spectroscopy package:[70]

$$I_{\mathrm{IR}}(m) = \sum_{\alpha} \left| \sum_{\kappa} \sum_{\beta} Z^*_{\kappa,\alpha\beta} X_{\kappa,\beta}(m) \right|^2 \quad (1)$$

Phonon assignments were made taking into account both the phonon frequency and the infrared intensity given by eq 1. We note that the phonon frequencies of $LuFeO_3$ and $ScFeO_3$ are slightly different (Tables S1 and S2) due to the different ionic sizes of the Lu and Sc cations. We expect the phonon frequencies in $Lu_{0.6}Sc_{0.4}FeO_3$ to lie between those of the two end-member compounds.

ASSOCIATED CONTENT

Supporting Information

The Supporting Information is available free of charge at https://pubs.acs.org/doi/10.1021/acsami.2c19600.

Calculated phonon frequencies for the $P6_3mc$ phase of $LuFeO_3$ and $ScFeO_3$ (Tables S1 and S2), detailed explanation of sample mapping (Figure S1), and investigation of domain-wall conductance (Figure S2) (PDF)

AUTHOR INFORMATION

Corresponding Author

Janice L. Musfeldt − *Department of Chemistry, University of Tennessee, Knoxville, Tennessee 37996, United States; Department of Physics and Astronomy, University of Tennessee, Knoxville, Tennessee 37996, United States;* orcid.org/0000-0002-6241-823X; Email: musfeldt@utk.edu

Authors

Kevin A. Smith − *Department of Chemistry, University of Tennessee, Knoxville, Tennessee 37996, United States*

Sriram P. Ramkumar − *Department of Materials Science and Engineering, University of California, Merced, California 95343, United States;* orcid.org/0000-0001-5410-7012

Kai Du − *Department of Physics and Astronomy, Rutgers University, Piscataway, New Jersey 08854, United States*

Xianghan Xu − *Department of Physics and Astronomy, Rutgers University, Piscataway, New Jersey 08854, United States*

Sang-Wook Cheong − *Department of Physics and Astronomy, Rutgers University, Piscataway, New Jersey 08854, United States; Rutgers Center for Emergent Materials, Rutgers University, Piscataway, New Jersey 08854, United States*

Stephanie N. Gilbert Corder − *Advanced Light Source Division, Lawrence Berkeley National Laboratory, Berkeley, California 94720, United States*

Hans A. Bechtel − *Advanced Light Source Division, Lawrence Berkeley National Laboratory, Berkeley, California 94720, United States*

Elizabeth A. Nowadnick − *Department of Materials Science and Engineering, University of California, Merced, California 95343, United States*

Complete contact information is available at: https://pubs.acs.org/10.1021/acsami.2c19600

Author Contributions

This project was conceived by J.L.M. and S.-W.C. The single crystals were grown and AFM + PFM mapping studies were carried out by K.D. and X.X. with advice from S.-W.C. The spectroscopic work was performed by K.A.S. with assistance from S.N.G.C., H.A.B., and J.L.M. The first-principles

https://doi.org/10.1021/acsami.2c19600
ACS Appl. Mater. Interfaces 2023, 15, 7562−7571

electronic structure calculations were carried out by S.P.R. with guidance from E.A.N. Data analysis was completed by K.A.S. with advice from J.L.M. All authors discussed the findings. The manuscript was written by K.A.S. and J.L.M. All authors read and commented on the manuscript.

Notes

The authors declare no competing financial interest.

■ ACKNOWLEDGMENTS

Research at the University of Tennessee was supported by the Division of Materials Research at the National Science Foundation (Grant DMR-2129904). The Advanced Light Source was supported by the Office of Basic Energy Sciences, Division of Materials Sciences and Engineering, of the U.S. Department of Energy under Contract DE-AC02-05CH11231. The work at Rutgers was supported by the Center for Quantum Materials Synthesis, funded by the Gordon and Betty Moore Foundation's EPiQS initiative through Grant GBMF10104, and by Rutgers University. This research used resources of the Center for Functional Nanomaterials, which is a U.S. DOE Office of Science Facility, and the Scientific Data and Computing Center, a component of the Computational Science Initiative, at Brookhaven National Laboratory under Contract No. DE-SC0012704.

■ REFERENCES

(1) Chae, S. C.; Horibe, Y.; Jeong, D. Y.; Rodan, S.; Lee, N.; Cheong, S.-W. Self-Organization, Condensation, and Annihilation of Topological Vortices and Antivortices in a Multiferroic. *Proc. Natl. Acad. Sci. U. S. A.* **2010**, *107*, 21366−21370.

(2) Jungk, T.; Hoffmann, Á.; Fiebig, M.; Soergel, E. Electrostatic Topology of Ferroelectric Domains in $YMnO_3$. *Appl. Phys. Lett.* **2010**, *97*, 012904.

(3) Choi, T.; Horibe, Y.; Yi, H. T.; Choi, Y. J.; Wu, W.; Cheong, S.-W. Insulating Interlocked Ferroelectric and Structural Antiphase Domain Walls in Multiferroic $YMnO_3$. *Nat. Mater.* **2010**, *9*, 253−258.

(4) Meier, D.; Seidel, J.; Cano, A.; Delaney, K.; Kumagai, Y.; Mostovoy, M.; Spaldin, N. A.; Ramesh, R.; Fiebig, M. Anisotropic Conductance at Improper Ferroelectric Domain Walls. *Nat. Mater.* **2012**, *11*, 284−288.

(5) Seidel, J. Domain Walls as Nanoscale Functional Elements. *J. Phys. Chem. Lett.* **2012**, *3*, 2905−2909.

(6) Han, M.-G.; Zhu, Y.; Wu, L.; Aoki, T.; Volkov, V.; Wang, X.; Chae, S. C.; Oh, Y. S.; Cheong, S.-W. Ferroelectric Switching Dynamics of Topological Vortex Domains in a Hexagonal Manganite. *Adv. Mater.* **2013**, *25*, 2415−2421.

(7) Fennie, C. J.; Rabe, K. M. Ferroelectric Transition in $YMnO_3$ from First Principles. *Phys. Rev. B* **2005**, *72*, 100103.

(8) Van Aken, B. B.; Palstra, T. T.; Filippetti, A.; Spaldin, N. A. The Origin of Ferroelectricity in Magnetoelectric $YMnO_3$. *Nat. Mater.* **2004**, *3*, 164−170.

(9) Artyukhin, S.; Delaney, K. T.; Spaldin, N. A.; Mostovoy, M. Landau Theory of Topological Defects in Multiferroic Hexagonal Manganites. *Nat. Mater.* **2014**, *13*, 42−49.

(10) Geng, Y.; Lee, N.; Choi, Y. J.; Cheong, S.-W.; Wu, W. Collective Magnetism at Multiferroic Vortex Domain Walls. *Nano Lett.* **2012**, *12*, 6055−6059.

(11) Geng, Y.; Das, H.; Wysocki, A. L.; Wang, X.; Cheong, S.-W.; Mostovoy, M.; Fennie, C. J.; Wu, W. Direct Visualization of Magnetoelectric Domains. *Nat. Mater.* **2014**, *13*, 163−167.

(12) Kumagai, Y.; Spaldin, N. A. Structural Domain Walls in Polar Hexagonal Manganites. *Nat. Commun.* **2013**, *4*, 1540.

(13) Evans, D. M.; Garcia, V.; Meier, D.; Bibes, M. Domains and Domain Walls in Multiferroics. *Physical Sciences Reviews* **2020**, *5*, 20190067.

(14) Sun, Q.-C.; Song, T.; Anderson, E.; Brunner, A.; Förster, J.; Shalomayeva, T.; Taniguchi, T.; Watanabe, K.; Gräfe, J.; Stöhr, R.; Xu, X.; Wrachtrup, J. Magnetic Domains and Domain Wall Pinning in Atomically Thin $CrBr_3$ Revealed by Nanoscale Imaging. *Nat. Commun.* **2021**, *12*, 1989.

(15) Alliati, I. M.; Evans, R. F. L.; Novoselov, K. S.; Santos, E. J. G. Relativistic Domain-Wall Dynamics in Van der Waals Antiferromagnet $MnPS_3$. *npj Comput. Mater.* **2022**, *8*, 3.

(16) Zhang, H.-Y.; Song, X.-J.; Chen, X.-G.; Zhang, Z.-X.; You, Y.-M.; Tang, Y.-Y.; Xiong, R.-G. Observation of Vortex Domains in a Two-Dimensional Lead Iodide Perovskite Ferroelectric. *J. Am. Chem. Soc.* **2020**, *142*, 4925−4931.

(17) Jakobsen, V. B.; Trzop, E.; Gavin, L. C.; Dobbelaar, E.; Chikara, S.; Ding, X.; Esien, K.; Müller-Bunz, H.; Felton, S.; Zapf, V. S.; Collet, E.; Carpenter, M. A.; Morgan, G. G. Stress-Induced Domain Wall Motion in a Ferroelastic Mn^{3+} Spin Crossover Complex. *Angew. Chem.* **2020**, *132*, 13407−13414.

(18) Choe, D.-H.; Kim, S.; Moon, T.; Jo, S.; Bae, H.; Nam, S.-G.; Lee, Y. S.; Heo, J. Unexpectedly Low Barrier of Ferroelectric Switching in HfO_2 via Topological Domain Walls. *Mater. Today* **2021**, *50*, 8−15.

(19) Cheng, Y.; Gao, Z.; Ye, K. H.; Park, H. W.; Zheng, Y.; Zheng, Y.; Gao, J.; Park, M. H.; Choi, J.-H.; Xue, K.-H.; Hwang, C. S.; Lyu, H. Reversible Transition Between the Polar and Antipolar Phases and its Implications for Wake-Up and Fatigue in HfO_2-Based Ferroelectric Thin Film. *Nat. Commun.* **2022**, *13*, 645.

(20) Wu, X.; Du, K.; Zheng, L.; Wu, D.; Cheong, S.-W.; Lai, K. Microwave Conductivity of Ferroelectric Domains and Domain Walls in a Hexagonal Rare-Earth Ferrite. *Phys. Rev. B* **2018**, *98*, 081409.

(21) Du, K.; Gao, B.; Wang, Y.; Xu, X.; Kim, J.; Hu, R.; Huang, F.-T.; Cheong, S.-W. Vortex Ferroelectric Domains, Large-Loop Weak Ferromagnetic Domains, and Their Decoupling in Hexagonal (Lu, Sc)FeO_3. *npj Quantum Mater.* **2018**, *3*, 33.

(22) White, J.; Sinha, K.; Xu, X. Structural Phase Diagram and Magnetic Properties of Sc-Substituted Rare Earth Ferrites $R_{1-x}Sc_xFeO_3$ (R = Lu, Yb, Er, and Ho). *J. Appl. Phys.* **2019**, *125*, 244101.

(23) Sinha, K.; Zhang, Y.; Jiang, X.; Wang, H.; Wang, X.; Zhang, X.; Ryan, P. J.; Kim, J.-W.; Bowlan, J.; Yarotski, D. A.; Li, Y.; DiChiara, A. D.; Cheng, X.; Wu, X.; Xu, X. Effects of Biaxial Strain on the Improper Multiferroicity in $LuFeO_3$ Films Studied Using the Restrained Thermal Expansion Method. *Phys. Rev. B* **2017**, *95*, 094110.

(24) Disseler, S. M.; Luo, X.; Gao, B.; Oh, Y. S.; Hu, R.; Wang, Y.; Quintana, D.; Zhang, A.; Huang, Q.; Lau, J.; Paul, R.; Lynn, J. W.; Cheong, S.-W.; Ratcliff, W. Multiferroicity in Doped Hexagonal $LuFeO_3$. *Phys. Rev. B* **2015**, *92*, 054435.

(25) Oh, Y. S.; Luo, X.; Huang, F.-T.; Wang, Y.; Cheong, S.-W. Experimental Demonstration of Hybrid Improper Ferroelectricity and the Presence of Abundant Charged Walls in $(Ca,Sr)_3Ti_2O_7$ Crystals. *Nat. Mater.* **2015**, *14*, 407−413.

(26) Sinha, K.; Wang, H.; Wang, X.; Zhou, L.; Yin, Y.; Wang, W.; Cheng, X.; Keavney, D. J.; Cao, H.; Liu, Y.; Wu, X.; Xu, X. Tuning the Néel Temperature of Hexagonal Ferrites by Structural Distortion. *Phys. Rev. Lett.* **2018**, *121*, 237203.

(27) Smith, K. A.; Ramkumar, S. P.; Harms, N. C.; Clune, A. J.; Cheong, S.-W.; Liu, Z.; Nowadnick, E. A.; Musfeldt, J. L. Pressure-Induced Phase Transition and Phonon Softening in h-$Lu_{0.6}Sc_{0.4}FeO_3$. *Phys. Rev. B* **2021**, *104*, 094109.

(28) Wu, X.; Petralanda, U.; Zheng, L.; Ren, Y.; Hu, R.; Cheong, S.-W.; Artyukhin, S.; Lai, K. Low-Energy Structural Dynamics of Ferroelectric Domain Walls in Hexagonal Rare-Earth Manganites. *Sci. Adv.* **2017**, *3*, No. e1602371.

(29) Holtz, M. E.; Padgett, E. S.; Steinhardt, R.; Brooks, C. M.; Meier, D.; Schlom, D. G.; Muller, D. A.; Mundy, J. A. Dimensionality-Induced Change in Topological Order in Multiferroic Oxide Superlattices. *Phys. Rev. Lett.* **2021**, *126*, 157601.

(30) Leiner, J. C.; Kim, T.; Park, K.; Oh, J.; Perring, T. G.; Walker, H. C.; Xu, X.; Wang, Y.; Cheong, S.-W.; Park, J.-G. Magnetic

https://doi.org/10.1021/acsami.2c19600
ACS Appl. Mater. Interfaces 2023, 15, 7562−7571

Excitations in the Bulk Multiferroic Two-Dimensional Triangular Lattice Antiferromagnet (Lu, Sc)FeO_3. *Phys. Rev. B* **2018**, *98*, 134412.
(31) Fan, S.; Singh, S.; Xu, X.; Park, K.; Qi, Y.; Cheong, S. W.; Vanderbilt, D.; Rabe, K. M.; Musfeldt, J. L. Vibrational Fingerprints of Ferroelectric HfO_2. *npj Quantum Mater.* **2022**, *7*, 32.
(32) Muller, E. A.; Pollard, B.; Raschke, M. B. Infrared Chemical Nano-Imaging: Accessing Structure, Coupling, and Dynamics on Molecular Length Scales. *J. Phys. Chem. Lett.* **2015**, *6*, 1275−1284.
(33) Mastel, S.; Govyadinov, A. A.; Maissen, C.; Chuvilin, A.; Berger, A.; Hillenbrand, R. Understanding the Image Contrast of Material Boundaries in IR Nanoscopy Reaching 5 nm Spatial Resolution. *ACS Photonics* **2018**, *5*, 3372−3378.
(34) Bechtel, H. A.; Johnson, S. C.; Khatib, O.; Muller, E. A.; Raschke, M. B. Synchrotron Infrared Nano-Spectroscopy and -Imaging. *Surf. Sci. Rep.* **2020**, *75*, 100493.
(35) Khatib, O.; Bechtel, H. A.; Martin, M. C.; Raschke, M. B.; Carr, G. L. Far Infrared Synchrotron Near-Field Nanoimaging and Nanospectroscopy. *ACS Photonics* **2018**, *5*, 2773−2779.
(36) Smith, K. A.; Nowadnick, E. A.; Fan, S.; Khatib, O.; Lim, S. J.; Gao, B.; Harms, N. C.; Neal, S. N.; Kirkland, J. K.; Martin, M. C.; Won, C. J.; Raschke, M. B.; Cheong, S.-W.; Fennie, C. J.; Carr, G. L.; Bechtel, H. A.; Musfeldt, J. L. Infrared Nano-Spectroscopy of Ferroelastic Domain Walls in Hybrid Improper Ferroelectric $Ca_3Ti_2O_7$. *Nat. Commun.* **2019**, *10*, 5235.
(37) McLeod, A. S.; Wieteska, A.; Chiriaco, G.; Foutty, B.; Wang, Y.; Yuan, Y.; Xue, F.; Gopalan, V.; Chen, L. Q.; Mao, Z. Q.; Millis, A. J.; Pasupathy, A. N.; Basov, D. N. Nano-Imaging of Strain-Tuned Stripe Textures in a Mott Crystal. *npj Quantum Mater.* **2021**, *6*, 46.
(38) Vitalone, R. A.; Sternbach, A. J.; Foutty, B. A.; McLeod, A. S.; Sow, C.; Golez, D.; Nakamura, F.; Maeno, Y.; Pasupathy, A. N.; Georges, A.; Millis, A. J.; Basov, D. N. Nanoscale Femtosecond Dynamics of Mott Insulator $(Ca_{0.99}Sr_{0.01})_2RuO_4$. *Nano Lett.* **2022**, *22*, 5689−5697.
(39) Roy, K. Ultra-Low-Energy Non-Volatile Straintronic Computing Using Single Multiferroic Composites. *Appl. Phys. Lett.* **2013**, *103*, 173110.
(40) Mittal, S. A Survey of Techniques for Approximate Computing. *ACM Comput. Surv.* **2016**, *48*, 1−33.
(41) Royo, M.; Escorihuela-Sayalero, C.; Íñiguez, J.; Rurali, R. Ferroelectric Domain Wall Phonon Polarizer. *Physical Review Materials* **2017**, *1*, 051402.
(42) Zurek, W. H. Cosmological Experiments in Superfluid Helium? *Nature* **1985**, *317*, 505−508.
(43) Duong, D. L.; Han, G. H.; Lee, S. M.; Gunes, F.; Kim, E. S.; Kim, S. T.; Kim, H.; Ta, Q. H.; So, K. P.; Yoon, S. J.; Chae, S. J.; Jo, Y. W.; Park, M. H.; Chae, S. H.; Lim, S. C.; Choi, J. Y.; Lee, Y. H. Probing Graphene Grain Boundaries with Optical Microscopy. *Nature* **2012**, *490*, 235−239.
(44) Hao, Z.; Bechtel, H. A.; Kneafsey, T.; Gilbert, B.; Nico, P. S. Cross-Scale Molecular Analysis of Chemical Heterogeneity in Shale Rocks. *Sci. Rep.* **2018**, *8*, 2552.
(45) Eliseev, E. A.; Morozovska, A. N.; Kalinin, S. V.; Li, Y.; Shen, J.; Glinchuk, M. D.; Chen, L.-Q.; Gopalan, V. Surface Effect on Domain Wall Width in Ferroelectrics. *J. Appl. Phys.* **2009**, *106*, 084102.
(46) Guzelturk, B.; Mei, A. B.; Zhang, L.; Tan, L. Z.; Donahue, P.; Singh, A. G.; Schlom, D. G.; Martin, L. W.; Lindenberg, A. M. Light-Induced Currents at Domain Walls in Multiferroic $BiFeO_3$. *Nano Lett.* **2020**, *20*, 145−151.
(47) Sun, Q.-C.; Xi, X.; Wang, X.; Lee, N.; Mazumdar, D.; Smith, R. J.; Carr, G. L.; Cheong, S.-W.; Musfeldt, J. L. Spectroscopic Signatures of Domain Walls in Hexagonal $ErMnO_3$. *Phys. Rev. B* **2014**, *90*, 121303.
(48) Chrosch, J.; Salje, E. K. H. Temperature Dependence of the Domain Wall Width in $LaAlO_3$. *J. Appl. Phys.* **1999**, *85*, 722−727.
(49) Catalan, G.; Seidel, J.; Ramesh, R.; Scott, J. F. Domain Wall Nanoelectronics. *Rev. Mod. Phys.* **2012**, *84*, 119−156.
(50) Moreno, R.; Evans, R. F. L.; Khmelevskyi, S.; Muñoz, M. C.; Chantrell, R. W.; Chubykalo-Fesenko, O. Temperature-Dependent Exchange Stiffness and Domain Wall Width in Co. *Phys. Rev. B* **2016**, *94*, 104433.
(51) Seidel, J.; Martin, L. W.; He, Q.; Zhan, Q.; Chu, Y.-H.; Rother, A.; Hawkridge, M. E.; Maksymovych, P.; Yu, P.; Gajek, M.; Balke, N.; Kalinin, S. V.; Gemming, S.; Wang, F.; Catalan, G.; Scott, J. F.; Spaldin, N. A.; Orenstein, J.; Ramesh, R. Conduction at Domain Walls in Oxide Multiferroics. *Nat. Mater.* **2009**, *8*, 229−234.
(52) Seidel, J.; Maksymovych, P.; Batra, Y.; Katan, A.; Yang, S.-Y.; He, Q.; Baddorf, A. P.; Kalinin, S. V.; Yang, C.-H.; Yang, J.-C.; Chu, Y.-H.; Salje, E. K. H.; Wormeester, H.; Salmeron, M.; Ramesh, R. Domain Wall Conductivity in La-Doped $BiFeO_3$. *Phys. Rev. Lett.* **2010**, *105*, 197603.
(53) Maksymovych, P.; Seidel, J.; Chu, Y. H.; Wu, P.; Baddorf, A. P.; Chen, L.-Q.; Kalinin, S. V.; Ramesh, R. Dynamic Conductivity of Ferroelectric Domain Walls in $BiFeO_3$. *Nano Lett.* **2011**, *11*, 1906−1912.
(54) Guyonnet, J.; Gaponenko, I.; Gariglio, S.; Paruch, P. Conduction at Domain Walls in Insulating $Pb(Zr_{0.2}Ti_{0.8})O_3$ Thin Films. *Adv. Mater.* **2011**, *23*, 5377−5382.
(55) Stolichnov, I.; Feigl, L.; McGilly, L. J.; Sluka, T.; Wei, X.-K.; Colla, E.; Crassous, A.; Shapovalov, K.; Yudin, P.; Tagantsev, A. K.; Setter, N. Bent Ferroelectric Domain Walls as Reconfigurable Metallic-Like Channels. *Nano Lett.* **2015**, *15*, 8049−8055.
(56) Liu, L.; Xu, K.; Li, Q.; Daniels, J.; Zhou, H.; Li, J.; Zhu, J.; Seidel, J.; Li, J. Giant Domain Wall Conductivity in Self-Assembled $BiFeO_3$ Nanocrystals. *Adv. Funct. Mater.* **2021**, *31*, 2005876.
(57) Bartels, M.; Hagen, V.; Burianek, M.; Getzlaff, M.; Bismayer, U.; Wiesendanger, R. Impurity-Induced Resistivity of Ferroelastic Domain Walls in Doped Lead Phosphate. *J. Phys.: Condens. Matter* **2003**, *15*, 957−962.
(58) Vasudevan, R. K.; Wu, W.; Guest, J. R.; Baddorf, A. P.; Morozovska, A. N.; Eliseev, E. A.; Balke, N.; Nagarajan, V.; Maksymovych, P.; Kalinin, S. V. Domain Wall Conduction and Polarization-Mediated Transport in Ferroelectrics. *Adv. Funct. Mater.* **2013**, *23*, 2592−2616.
(59) Tagantsev, A. K.; Cross, L. E.; Fousek, J. *Domains in Ferroic Crystals and Thin Films*; Springer: New York, 2010.
(60) Yudin, P. V.; Gureev, M. Y.; Sluka, T.; Tagantsev, A. K.; Setter, N. Anomalously Thick Domain Walls in Ferroelectrics. *Phys. Rev. B* **2015**, *91*, 060102.
(61) Xu, T.; Shimada, T.; Araki, Y.; Wang, J.; Kitamura, T. Multiferroic Domain Walls in Ferroelectric $PbTiO_3$ With Oxygen Deficiency. *Nano Lett.* **2016**, *16*, 454−458.
(62) Seijas-Bellido, J. A.; Escorihuela-Sayalero, C.; Royo, M.; Ljungberg, M. P.; Wojdeł, J. C.; Íñiguez, J.; Rurali, R. A Phononic Switch Based on Ferroelectric Domain Walls. *Phys. Rev. B* **2017**, *96*, 140101.
(63) Yelisieiev, M.; Maksymovych, P.; Morozovska, A. N. Probing Phonon Softening in Ferroelectrics by Scanning Probe Microwave Spectroscopy. *Phys. Rev. B* **2021**, *104*, 174105.
(64) Bugallo, D.; Langenberg, E.; Ferreiro-Vila, E.; Smith, E. H.; Stefani, C.; Batlle, X.; Catalan, G.; Domingo, N.; Schlom, D. G.; Rivadulla, F. Deconvolution of Phonon Scattering by Ferroelectric Domain Walls and Point Defects in a $PbTiO_3$ Thin Film Deposited in a Composition-Spread Geometry. *ACS Appl. Mater. Interfaces* **2021**, *13*, 45679−45685.
(65) Kresse, G.; Furthmüller, J. Efficiency of Ab-Initio Total Energy Calculations for Metals and Semiconductors Using a Plane-Wave Basis Set. *Comput. Mater. Sci.* **1996**, *6*, 15−50.
(66) Liechtenstein, A. I.; Anisimov, V. I.; Zaanen, J. Density-Functional Theory and Strong Interactions: Orbital Ordering in Mott-Hubbard Insulators. *Phys. Rev. B* **1995**, *52*, R5467−R5470.
(67) Gonze, X.; Lee, C. Dynamical Matrices, Born Effective Charges, Dielectric Permittivity Tensors, and Interatomic Force Constants From Density-Functional Perturbation Theory. *Phys. Rev. B* **1997**, *55*, 10355−10368.
(68) Togo, A.; Oba, F.; Tanaka, I. First-Principles Calculations of the Ferroelastic Transition Between Rutile-Type and $CaCl_2$-Type SiO_2 at High Pressures. *Phys. Rev. B* **2008**, *78*, 134106.

https://doi.org/10.1021/acsami.2c19600
ACS Appl. Mater. Interfaces 2023, 15, 7562−7571

(69) Togo, A.; Chaput, L.; Tanaka, I. Distributions of Phonon Lifetimes in Brillouin Zones. *Phys. Rev. B* **2015**, *91*, 094306.
(70) Skelton, J. M.; Burton, L. A.; Jackson, A. J.; Oba, F.; Parker, S. C.; Walsh, A. Lattice Dynamics of the Tin Sulphides SnS_2, SnS and Sn_2S_3: Vibrational Spectra and Thermal Transport. *Phys. Chem. Chem. Phys.* **2017**, *19*, 12452−12465.

https://doi.org/10.1021/acsami.2c19600
ACS Appl. Mater. Interfaces 2023, 15, 7562−7571